Lindoo, A., Larsen, J. F., Cashman, K. V., Dunn, A. L., & Neill, O. K. (2016). An experimental study of permeability development as a function of crystal-free melt viscosity. *Earth and Planetary Science Letters*, *435*, 45-54. https://doi.org/10.1016/j.epsl.2015.11.035

An experimental study of permeability development as a function of crystal-free melt viscosity

A. Lindoo[a], J.F. Larsen[a], K.V. Cashman[b], A.L. Dunn[a], O.K. Neill[c]

[a]Geophysical Institute, University of Alaska Fairbanks, Fairbanks, Alaska 99775, USA
[b]School of Earth Sciences, University of Bristol, Bristol BS81RJ, UK
[c]Peter Hooper GeoAnalytical Laboratory, School of the Environment, Washington State University, Pullman, Washington 99164, USA

Corresponding author:
E-mail address: alindoo@alaska.edu (A.Lindoo)

Abstract

Permeability development in magmas controls gas escape and, as a consequence, modulates eruptive activity. To date, there are few experimental controls on bubble growth and permeability development, particularly in low viscosity melts. To address this knowledge gap, we have run controlled decompression experiments on crystal-free rhyolite (76 wt. % SiO_2), rhyodacite (70 wt. % SiO_2), K-phonolite (55 wt. % SiO_2) and basaltic andesite (54 wt. % SiO_2) melts. This suite of experiments allows us to examine controls on the critical porosity at which vesiculating melts become permeable. As starting materials we used both fine powders and solid slabs of pumice, obsidian and annealed starting materials with viscosities of ~10^2 to ~10^6 Pa s. We saturated the experiments with water at 900˚ (rhyolite, rhyodacite, and phonolite) and 1025˚C (basaltic andesite) at 150 MPa for 2-72 hours and decompressed samples isothermally to final pressures of 125 to 10 MPa at rates of 0.25-4.11 MPa/s. Sample porosity was calculated from reflected light images of polished charges and permeability was measured using a bench-top gas permeameter and application of the Forchheimer equation to estimate both viscous (k_1) and inertial (k_2) permeabilities. Degassing conditions were assessed by measuring dissolved water contents using micro-Fourier-Transform Infrared (μ-FTIR) techniques.

All experiment charges are impermeable below a critical porosity (ϕ_c) that varies among melt compositions. For experiments decompressed at 0.25 MPa s^{-1}, we find the percolation threshold for rhyolite is 68.3 ± 2.2 vol.%; for rhyodacite is 77.3 ± 3.8 vol.%; and for K-phonolite is 75.6 ± 1.9 vol.%. Rhyolite decompressed at 3-4 MPa s^{-1} has a percolation threshold of 74 ± 1.8 vol.%. These results are similar to previous experiments on silicic melts and to high permeability thresholds inferred for silicic pumice. All basaltic andesite melts decompressed at 0.25 MPa s^{-1}, in contrast, have permeabilities below the detection limit (~10^{-15} m^2), and a maximum porosity of 63 vol.%. Additionally, although the measured porosities of basaltic andesite experiments are ~10-35 vol. % lower than calculated equilibrium porosities, μ-FTIR analyses confirm the basaltic andesite melts remained in equilibrium during degassing. We show that the low porosities and permeabilities are a consequence of short melt relaxation timescales during syn- and post-decompression degassing. Our results suggest that basaltic andesite melts reached ϕ_c > 63 vol. % and subsequently degassed; loss of internal bubble pressure caused the bubbles to shrink and their connecting apertures to seal before quench, closing the connected pathways between bubbles. Our results challenge the hypothesis that low viscosity melts have a permeability threshold of ~30 vol. %, and instead support the high permeability thresholds observed in analogue experiments on low viscosity materials. Importantly, however, these low viscosity melts are unable to maintain high porosities once the percolation threshold is exceeded because of rapid outgassing and collapse of the permeable network. We conclude, therefore, that melt viscosity has little effect on percolation threshold development, but does influence outgassing.

Keywords: Vesiculation; Gas permeability; Viscosity; Decompression; Crystal-free melts

1. Introduction

Vesiculation of ascending magmas drives volcanic eruptions. The explosivity of an eruption is modulated by the physical state of the conduit (Jaupart, 1998) and the degassing efficiency of the magma, which may proceed either through permeable bubble networks (Rust and Cashman, 2004) or magma fracture along conduit walls (Gonnermann and Manga, 2007). In silicic melts, degassing via permeable networks has been studied through analysis of eruptive products and decompression experiments on natural and analog materials. However, few studies have attempted to quantify and describe permeability development in low viscosity melts, and no experimental studies have been conducted. To address this gap, we extend decompression experiments to mafic and alkalic compositions. By comparing these results with those of their silicic counterparts, we address the role of melt viscosity in modulating the degassing process.

Magmas become permeable via one or both of two processes: connection of bubbles via coalescence to form permeable networks (e.g., Wright et al., 2009) or magma fracture (Castro et al., 2012a). Here we focus on development of permeable bubble networks, which is more likely than magma fracture to facilitate wholesale magma degassing in the conduit. As magma ascends, decreasing pressure causes the melt to become supersaturated with H_2O (e.g., Stolper, 1982), which triggers bubble nucleation and growth via diffusion and expansion. Vesiculation and bubble expansion can generate high vesicularities (>70 vol. %) and form magmatic foams, as observed in natural pumice clasts (e.g., Klug and Cashman, 1996; Wright et al., 2009). Once the magmatic foam expands sufficiently to allow bubbles to impinge on one another, melt films separating neighboring bubbles thin and rupture to form apertures between bubbles. Extensive

coalescence can create a connected network of bubbles that acts as a passageway for volatiles to quickly exit the system. The vesicularity at which magma becomes permeable (critical porosity, ϕ_c) is termed the percolation threshold (Sahimi, 1994; Blower, 2001).

Bubble coalescence is primarily controlled by melt viscosity. In order for neighboring bubbles to coalesce, the melt films separating them must rupture; this is assumed to occur at a critical thickness (Proussevitch et al., 1993; Castro et al., 2012b). The timescales required to thin or stretch interstitial melt-films are controlled by melt viscosity and surface tension (Rust and Cashman, 2011). For this reason, coalescence occurs much more readily in lower viscosity melts; therefore, it has been assumed that the onset of permeability in mafic melts occurs at a lower porosity than in silicic melts.

Once degassing commences, bubbles may deform or shrink while still maintaining a permeable pathway. This results in a hysteresis effect where vesicularity decreases as a result of deformation and reduced overpressure, while connected bubble networks maintain streamlined passageways for permeable outgassing (Saar and Manga, 1999; Rust and Cashman, 2004; Rust and Cashman, 2011). Effusive products typically exhibit this hysteresis effect (e.g. Mueller et al. 2008), implying they achieved permeability and degassed. The extent to which permeability networks are modified during explosive eruptions is unknown.

Previous work examining critical porosities in phenocryst-poor, natural and experimental silicic (rhyolite and rhyodacite) pumice suggest percolation thresholds between 56 and 78 vol. % (Eichelberger et al., 1986; Klug and Cashman, 1996; Takeuchi et al., 2009). Theoretical models based on packing geometry of spheres (Blower, 2001), in contrast, predict permeability at porosities $\geq$ 30 vol. %. These predictions appear to be

47 supported by analysis of phenocryst-poor, basaltic scoriae (Saar and Manga, 1999),
48 where measurements at high porosities were fit by a curve calculated using percolation
49 theory (Sahimi, 1994). Crystal-poor basaltic melts in Hawaii, in contrast, commonly
50 produce pyroclasts with vesicularities >> 70 vol. % (Rust and Cashman, 2011); these data
51 are more consistent with an analog study that found permeability development to be
52 delayed until $\phi_c \approx 70$ vol. % in low viscosity corn syrup (Namiki and Manga, 2008). This
53 percolation threshold is significantly higher than the ~30 vol. % proposed by percolation
54 theory and more in line with results for natural and experimental crystal-free, high
55 viscosity, silicic melts. One possible explanation for this discrepancy lies in the high
56 micro-crystallinity of most analyzed scoria samples, and the potential role of crystals in
57 reducing the percolation threshold (Rust and Cashman, 2011), although decompression
58 experiments have yet to confirm this hypothesis (Okumura et al., 2012). Alternatively,
59 the discrepancy between theoretical and observed percolation thresholds may reflect
60 limitations in the models, which do not account for either bulk volume expansion or the
61 time required to thin films that separate individual bubbles (Rust and Cashman, 2011).
62 To better understand this problem, we use high pressure and temperature
63 decompression experiments to constrain critical porosities in phenocryst-free melts. The
64 experiments employ rhyolite, rhyodacite, K-rich phonolite, and basaltic andesite starting
65 materials to observe bubble exsolution and permeability development over melt
66 viscosities that vary over four orders of magnitude (10^2 to $10^{6.2}$ Pa s). The initial starting
67 conditions approximate water-saturated, supra-liquidus magma that is stored at
68 approximately 6 km depth in the crust and ascends rapidly (~10 to 300 m/s). The
69 resulting permeabilities are measured with a bench-top permeameter constructed for

small experimental samples. We find that percolation thresholds are similar for all melt compositions, but that melt viscosity exerts a profound influence on degassing and subsequent permeability development. We use these results to explore the role of magma viscosity in controlling syn-eruptive degassing and consequences for eruption styles.

2. Experimental and Analytical Methods

2.1. Experimental methods

Decompression experiments employed both continuous and step-wise decompression pathways. Sample materials included powders and solid slabs of glassy rhyolite, rhyodacite, K-rich phonolite, and basaltic andesite from (Table 1): rhyolite (Mono Craters, CA; 76.32 wt.% SiO_2), rhyodacite (Aniakchak; 70.57 wt.% SiO_2; Larsen et al., 2006), K-phonolite (79 AD Vesuvius; 55.41 wt.% SiO_2; Shea et al., 2010a), and basaltic andesite (Okmok; 54.82 wt.% SiO_2; Wong and Larsen, 2010). These melt compositions were selected to encompass a wide range of estimated melt viscosities, and because the phase equilibria are known from previous experiments.

Initially all experiments were conducted using powders from natural pumice (Aniakchak rhyodacite, 79 AD Vesuvius phonolite), obsidian (Mono Craters rhyolite), or twice fused glassy lava (Okmok vitreous basaltic andesite). Using finely ground powders allows the initial diffusion timescale to be short, alleviating hydrogen loss through the capsules in the Ar pressurized TZM runs. It also mitigates the potential for Fe-loss to the capsule. Because it is known that powdered starting materials contain an inherited set of large “hydration” bubbles (Larsen and Gardner, 2000), a second set of experiments were run for the Mono Craters rhyolite and Okmok basaltic andesite compositions using solid

93 slabs as the starting materials. These experiments allow us to correct for “hydration
94 bubbles” in the powder samples (e.g., Gardner et al., 1999; Larsen and Gardner, 2000).
95 Experiments were conducted using TZM (titanium-zirconium-molybdenum alloy)
96 and MHC (molybdenum-hafnium-carbide alloy) vessels pressurized with ultra-high
97 purity Ar gas, with ~2.5 bars CH_4 added to mitigate H diffusion. The charges were
98 compressed with the Ar-CH_4 mixture to an initial pressure of 150 MPa, lowered into a
99 Deltech furnace and heated to 900°C (rhyolite, rhyodacite, phonolite) or 1025°C (basaltic
100 andesite). Pressure was monitored using a Heise pressure gauge accurate to ±1MPa,
101 according to the manufacturer specifications. Experimental capsules were held first at
102 150 MPa for 2 to 72 hours, with the hold times determined by calculating water
103 diffusivities as a function of the average powder grain sizes or slab dimensions, to ensure
104 that the experimental melts were H_2O-saturated before decompression (see Appendix A).
105 Samples were isothermally decompressed continuously or using step-wise pathways for
106 rates between 0.25 - 6 MPa/s. Once final pressures of 125, 100, 75, 50, 35, 25, 15, or 10
107 MPa were reached (see Appendix A, Table S1), the vessel was pulled from the furnace
108 and inverted, dropping the capsule against the water-cooled jacket surrounding the
109 pressure connection to quench within a few seconds.
110
111 *2.2. Permeability measurement*
112 Samples were extracted as whole, unbroken slugs from their capsules using a
113 razor blade and wire cutters. The samples were then wrapped in high viscosity
114 Crystalbond 509 to seal the outside surface, and then submerged in 30 mL cups filled
115 with Hillquist epoxy. After curing overnight, the samples were separated from the plastic

cups for cutting and polishing (after Takeuchi et al., 2008). Cross-sectional areas of the experiments were exposed by polishing down the top and bottom of the plugs until the surfaces were parallel and no thinner than 10x the largest bubble diameter (Blower, 2001).

A gas permeameter was built at University of Alaska-Fairbanks following the design of Takeuchi et al., (2008) to measure permeabilities of small experimental samples (see Appendix A). The experimental samples were measured at a range of gas flow rates and upstream air pressures to create a curve that could be fitted using a modified version of Darcy's Law, the Forcheimer equation, to solve for viscous (k_1) and inertial permeabilities (k_2; Rust and Cashman, 2004).

(1) $$\frac{P_2^2 - P_1^2}{2P_0 L} = \frac{\mu}{k_1} v + \frac{\rho}{k_2} v^2 ,$$

The Forchheimer equation is preferred for vesicular silicic samples because it accounts for energy loss through inertial effects as flow rate increases (Rust and Cashman, 2004). The k_1 and k_2 permeabilities can be calculated from the data by fitting a second order polynomial to the calculated modified pressure gradient and gas volume flux derived from permeability measurements (e.g., Rust and Cashman, 2004; Takeuchi et al., 2008). Each experiment was measured three times over the full range of gas flow rates to determine reproducibility. These repeat measurements produced standard deviations that are typically 0.1 log units (k_1) and 0.27 log units (k_2). The fitting error of the second order polynomial for all samples was $R^2 \geq 0.998$ (see Appendix A, Fig.S1).

2.3. Vesicularity

139 To determine total vesicularity, reflected light images were taken of sample cross-
140 sections exposed for permeameter measurements. The photomicrographs were processed
141 in Adobe Photoshop to be converted to binary images (Appendix A). Errors in
142 vesicularity were determined by averaging measurements obtained from multiple regions
143 of interest and calculating the standard deviation about the mean. In samples comprising
144 a single image, errors were determined by reprocessing and analyzing the same image
145 three times. These images were then input into a Matlab-based program (FOAMs, Shea et
146 al., 2010b) to quantify bubble size and number.
147
148 *2.4. FTIR analyses*
149 Dissolved water contents were measured using a Thermo Fisher Scientific 6700
150 Fourier Transform Infrared Spectrometer coupled with a continuum microscope with two
151 MCT-A detectors, one standard and one 50 micron for higher resolution analyses from
152 smaller apertures (King et al., 2004)(see Appendix A). A purge collar was used to
153 minimize the interference of atmospheric water and CO_2 on the analyses. Samples were
154 placed on a NaCl disk for transmission analyses, which were acquired over a
155 wavenumber range of $\tilde{\nu}$ = 6500 - 650 cm^{-1} with the aperture set to 20 x 20 μm.
156 Background spectra were collected before each analysis through the NaCl disk adjacent
157 to the sample. Water concentrations were measured from 3 to 4 spots on each sample,
158 with each spectra consisting of 512 scans at a resolution of 4 cm^{-1}.
159

3. Results

3.1. Experimental porosities

All experiments yielded crystal-free, vesicular glasses. Large vesicles (72 to 280 μm in diameter) present in experiments employing powdered starting materials and quenched at high final pressures (P_f = 126 MPa) most likely represent hydration bubbles (e.g., Gardner et al., 1999; Larsen and Gardner, 2000). The porosities of all experimental series systematically increase as a function of decreasing final pressure (Fig. 1a). Experimental porosities in runs that used rhyolitic or phonolitic powdered starting materials (see Appendix A, Table S1) are consistently higher than equilibrium calculated from solubility curves (Moore et al., 1998) (Fig. 1b; Equation 2), and are probably the result of hydration bubbles. In contrast, experiments using basaltic andesite starting compositions, both powdered and solid slab, produce experimental porosities that are systematically less than predicted by equilibrium, and indicate gas loss during decompression.

A comparison of calculated equilibrium porosities with measured porosities determined from photomicrographs as a function of final pressures (Fig. 1b) confirms the role of hydration bubbles, as determined using the analysis of Gardner et al. (1999):

$$\phi M = \left[\frac{\frac{\rho_m}{Z} V_w (\omega_o - \omega_F)}{1 + \left(\frac{\rho_M}{Z} V_w (\omega_o - \omega_F)\right)}\right], \quad (2)$$

where ρ_m is the melt density, Z is the molecular weight of water, V_w is the molar volume of water at final pressure, and ω_0 and ω_F the weight fractions of dissolved water at initial and final pressure, respectively.

Figure 1a

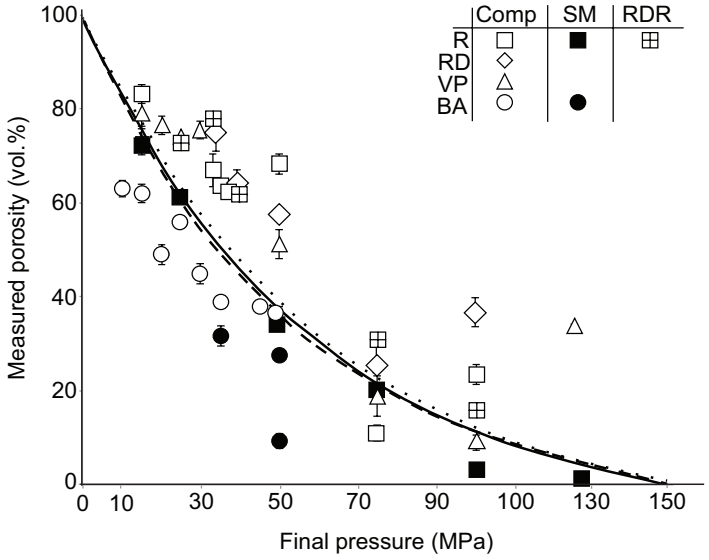

Figure 1b

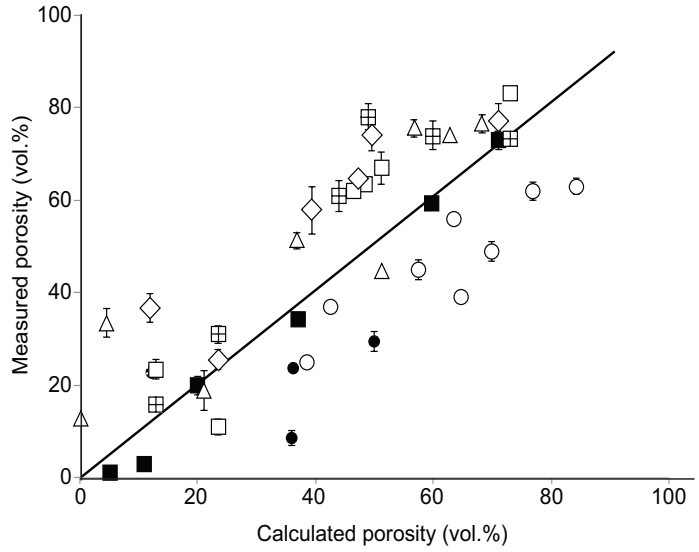

Fig. 1a: Measured porosity as a function of final quench pressure. The dashed, solid, and dotted lines represent equilibrium rhyolite, K-phonolite, and basaltic andesite porosities. Legend: sample compositions (COMP) are denoted by open squares (rhyolite), diamonds (rhyodacite), triangles (K-phonolite) and circles (basaltic andesite). Samples using solid slab starting materials (SM) are indicated by filled in symbols. Rhyolite samples that underwent rapid decompression rates (RDR) are marked with an internal cross. Silicic samples with powdered starting material are in general in agreement or above calculated equilibrium porosities. Samples with solid slab (SS) starting material track calculated equilibrium porosities. Basaltic andesite samples using solid slab and powdered starting materials all have porosities lower than expected at equilibrium

Fig. 1b: A comparison of measured porosities determined from photomicrographs to equilibrium porosities calculated using equation (2). Error bars denote standard deviation (σ) of replicate porosity measurements.

183 *3.2. Water concentrations in the experimental glasses*

184 The extent to which degassing occurred at equilibrium can be determined using
185 micro-FTIR transmission spectroscopy methods and predicted solubility curves (Fig. 2;
186 Moore et al., 1998). The rhyolite glasses using powdered starting material decompressed
187 step-wise at 0.25 MPa/s have water contents (H_2O_{tot}) ranging from 3.80±0.03 to
188 2.34±0.02 wt. % at P_F = 75 and 15 MPa, respectively (See Appendix A). Total water
189 concentrations analyzed in the K-phonolite glasses from powdered starting materials
190 range from 4.37±0.05 wt. % to 2.41±0.02 wt. % at P_F = 150 and 50 MPa, respectively.
191 The basaltic andesite experimental glasses have H_2O_{tot} from 2.18±0.18 wt. % to
192 1.18±0.06 wt. % at P_F = 45 and 15 MPa final pressures. Rhyolite glasses from powdered
193 starting material decompressed step-wise at 0.25 MPa are H_2O oversaturated by 0.09 to 2
194 wt. % water at P_F= 75 to 15. K-phonolite and basaltic andesite experimental glasses have
195 H_2O concentrations that are in agreement with their respective solubility curves. Our
196 rhyolite data are comparable to experiments by Gardner et al. (1999), who found that
197 rhyolite glasses decompressed to P_F = 140 to 100 MPa at 0.25 MPa/s were enriched in
198 H_2O_{tot} by 0.33 to 1 wt. % relative to the predicted solubility curve.

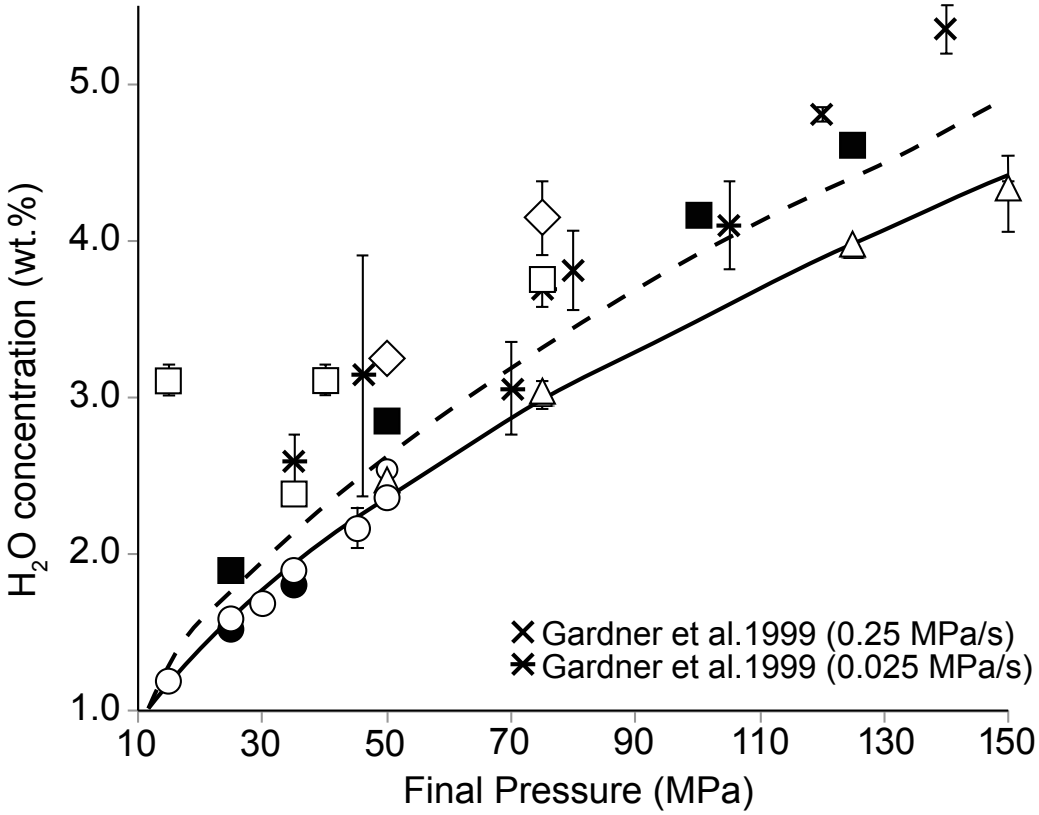

Fig. 2: Total water content in experimental samples measured using FTIR. We use the same symbols as figure 1 with the exception of those represented in the legend. The dashed curve represents predicted equilibrium water concentrations for rhyolite and rhyodacite melt compositions (Moore et al., 1998). The solid line represents equilibrium water concentrations in K-phonolite and basaltic andesite melts (Moore et al., 1998). Rhyolite and rhyodacite water concentrations are typically similar to or above equilibrium concentrations, while K-phonolite and basaltic andesite melts show water concentrations in agreement with equilibrium. A previous study by Gardner et al. (1999) is plotted to compare water oversaturation seen in rhyolites decompressed at similar rates.

199 *3.3. Experimental permeabilities*

200 Permeabilities of all experiments are below the detection limit of our
201 permeameter (~10^{-15} m^2) until they reach a critical porosity (ϕ_c; Fig. 3a) at which their
202 permeabilities become measurable. The Darcian (viscous) permeability (k_1) of rhyolite
203 melts decompressed continuously between 2.5 and 4.11 MPa/s becomes measureable at
204 ϕ_c=74 vol. %, while rhyolitic melts decompressed step-wise at 0.25 MPa/s become
205 permeable at ϕ_c between 65 - 80 vol. % porosity. Rhyodacite decompressed step-wise at
206 0.25 MPa/s is permeable at ϕ_c ~64 vol. % and K-phonolite decompressed step-wise at
207 0.25 MPa/s at 76 vol. %. In contrast, the basaltic andesite experiments decompressed
208 continuously at 0.25 MPa/s remain below the permeameter detection limit to pressures as
209 low as 10 MPa, with porosity = 63 vol. %.

210 Non-Darcian (inertial) permeability (k_2) of rhyolite melts decompressed
211 continuously between 2.5 and 4.11 MPa/s is measurable within a range of 74-78 vol. %
212 porosity (Fig. 3b). Decompressed step-wise at 0.25 MPa/s, rhyolite inertial permeabilities
213 become measurable and range between -11.29 (0.22) to -8.73 (0.13) when experiments
214 reach 66 and 83.2 vol.% porosity. Permeability resulting from step-wise decompression
215 of rhyolite at the same rate reaches log k_2 = -7.79 (0.08) m at ϕ_c ~ 60 vol. % porosity. K-
216 phonolite decompressed step-wise at 0.25 MPa/s reaches log k_2 = -8.81 (0.01) m at ~76
217 vol.% porosity. Inertial permeabilities of basaltic andesite melts decompressed
218 continuously are below the detection limit of the permeameter. A comparison of k_1 and k_2
219 yields a power-law trend that is similar to those found in previous experimental and
220 natural studies (Fig.4)(Rust and Cashman, 2004; Wright et al., 2007; Takeuchi et al.,
221 2009; Polacci et al., 2014). Interestingly, the experimental samples span most of the k_1/k_2

222 range covered by the natural samples. This would imply that the scale of the porous

223 media does not affect the ratio of k_1/k_2.

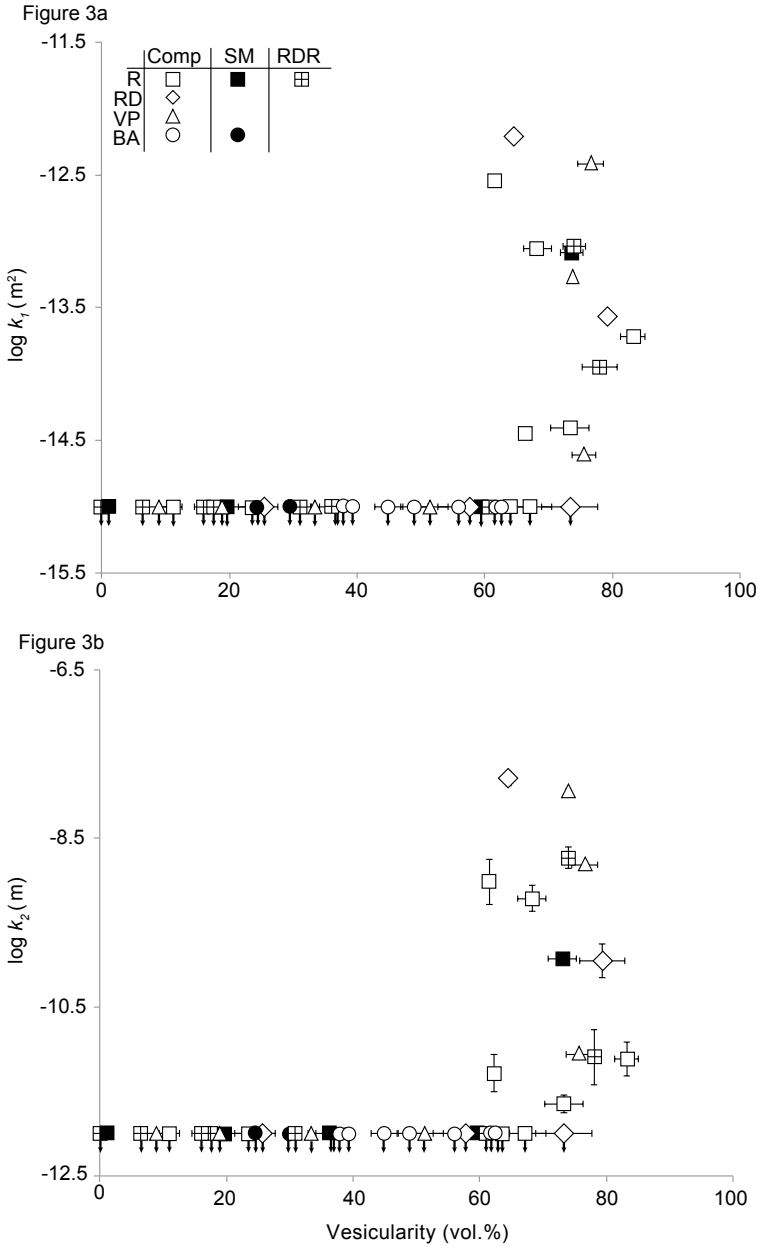

Fig. 3a: Relationship between vesicularity and viscous (k_1) permeability. Fig. 3b: Inertial permeability as a function of vesicularity. Symbols are the same as figures 1 and 2. Down arrows indicate the detection limit of the permeameter, therefore permeabilities are lower than the plotted values. Standard deviations are smaller than symbols unless otherwise noted.

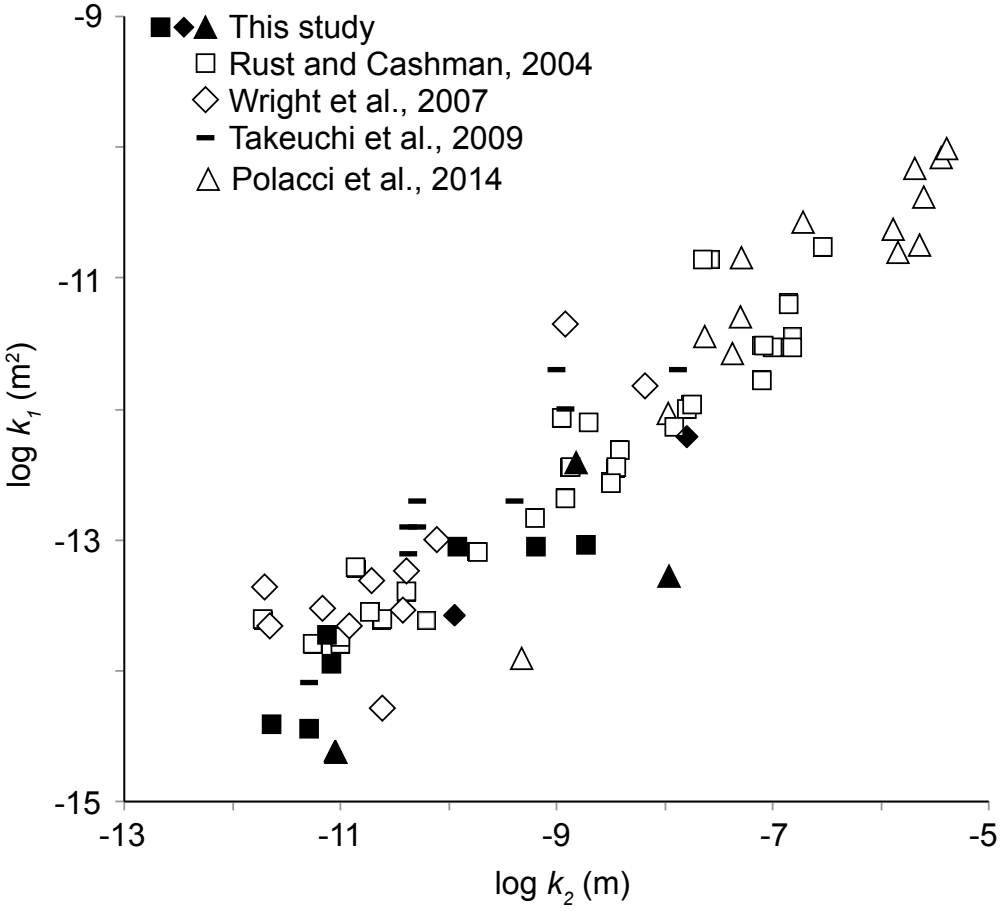

Fig. 4: Viscous (k_1) vs. inertial permeability (k_2). The shapes of the symbols indicate sample composition following the labeling strategy as previous figures. This study as well as another experimental study, Takeuchi et al., (2009), are marked by black symbols. Studies on pumice are indicated with open or light gray symbols.

4. Discussion

4.1. Permeability development in rhyolite, rhyodacite and K-phonolite melts

The permeabilities of silicic samples measured in this investigation compare well with available data on rhyolite decompression experiments from Takeuchi et al. (2009). Our experiments predict percolation thresholds that are generally consistent with, but slightly lower than the experimental studies of Takeuchi et al. (2009) and higher than those of Westrich and Eichelberger (1994). As seen in previous studies, we observe an abrupt increase in permeability at a critical porosity below which permeabilities were not detectable ($k_1 < \log k_l = 10^{-15}$ m^2). If we take this as the percolation threshold, then ϕ_c for rhyolite is 68.3 ± 2.2 vol.%; for rhyodacite is 77.3 ± 3.8 vol.%; and for K-phonolite is 75.6 ± 1.9 vol.% (Fig. 3). Rhyolite decompressed at 3-4 MPa/s has a percolation threshold of 74 ± 1.8 vol.%.

Our percolation thresholds are lower than the 80 vol.% defined by Takeuchi et al., (2009), despite similar melt compositions. The most obvious difference is the decompression rate. Takeuchi et al., (2009) found no rate dependence for decompression rates ranging from 0.002 to 0.05 MPa/s. Slower decompression rates leave more time for coalescence processes such as melt film thinning and rupture, the receding of bubble walls and widening of bubble apertures (Rust and Cashman, 2004; Burgisser and Gardner, 2004; Mueller et al., 2008; Takeuchi et al., 2009; Kobayashi et al., 2010; Castro et al., 2012b). Although our decompression rates are significantly faster, the apparent percolation threshold increases with increasing decompression rate, and thus cannot fully account for the observed difference. From this comparison we conclude that more data

246 are needed to determine whether percolation threshold development is rate dependent,
247 although the results of rhyolitic experiments imply it is a possibility.

248 The difference in percolation thresholds may be due to experimental methods.
249 Although both Takeuchi et al., (2009) and this study use powdered starting materials,
250 Takeuchi et al., (2009) held the samples for one day before decompression. Hydration
251 bubbles were likely able to rise out of the sample during that time period (see section
252 4.3.). Although hydration bubbles do not appear to affect the percolation threshold, they
253 will affect the bubble size distribution. Vesicle size distributions measured from the four
254 compositional series (Fig. 5) illustrate the resulting vesicle size distributions when
255 hydration bubbles form. Experiments from powdered starting material feature vesicle
256 sizes that are generally greater than 18 μm diameter, while solid slab starting materials
257 include vesicles below that threshold. The abundance of larger bubbles in the powdered
258 experiments could have encouraged bubble-bubble interaction, particularly to the extent
259 that coalescence is aided by contrasting internal pressures between small and large
260 bubbles.

261 Sample permeabilities have also been calculated using lattice Boltzmann models
262 on X-ray computed microtomography (XRCT) images of experimental samples. These
263 studies suggest that permeability may develop at porosities as low as 49 vol. % in rhyolite
264 and 29 vol. % in basalt (Bai et al., 2010; Martel and Iacono-Marziano, 2015).
265 Importantly, for a given porosity, the calculated permeabilities are consistently higher
266 than those obtained from direct measurements. This mismatch may arise from the voxel
267 resolution (cubic voxel edge length ~1.85-9 μm) (Bai et al., 2010; Polacci et al., 2012),
268 which cannot image the thin bubble walls ($\leq$1 micron) typical of rhyolitic samples, in

269 particular (e.g., Klug et al., 2002). Bubble walls below the detection limit would then
270 appear as pore apertures in lattice Boltzmann calculations, with the result being
271 artificially high estimates of permeability.

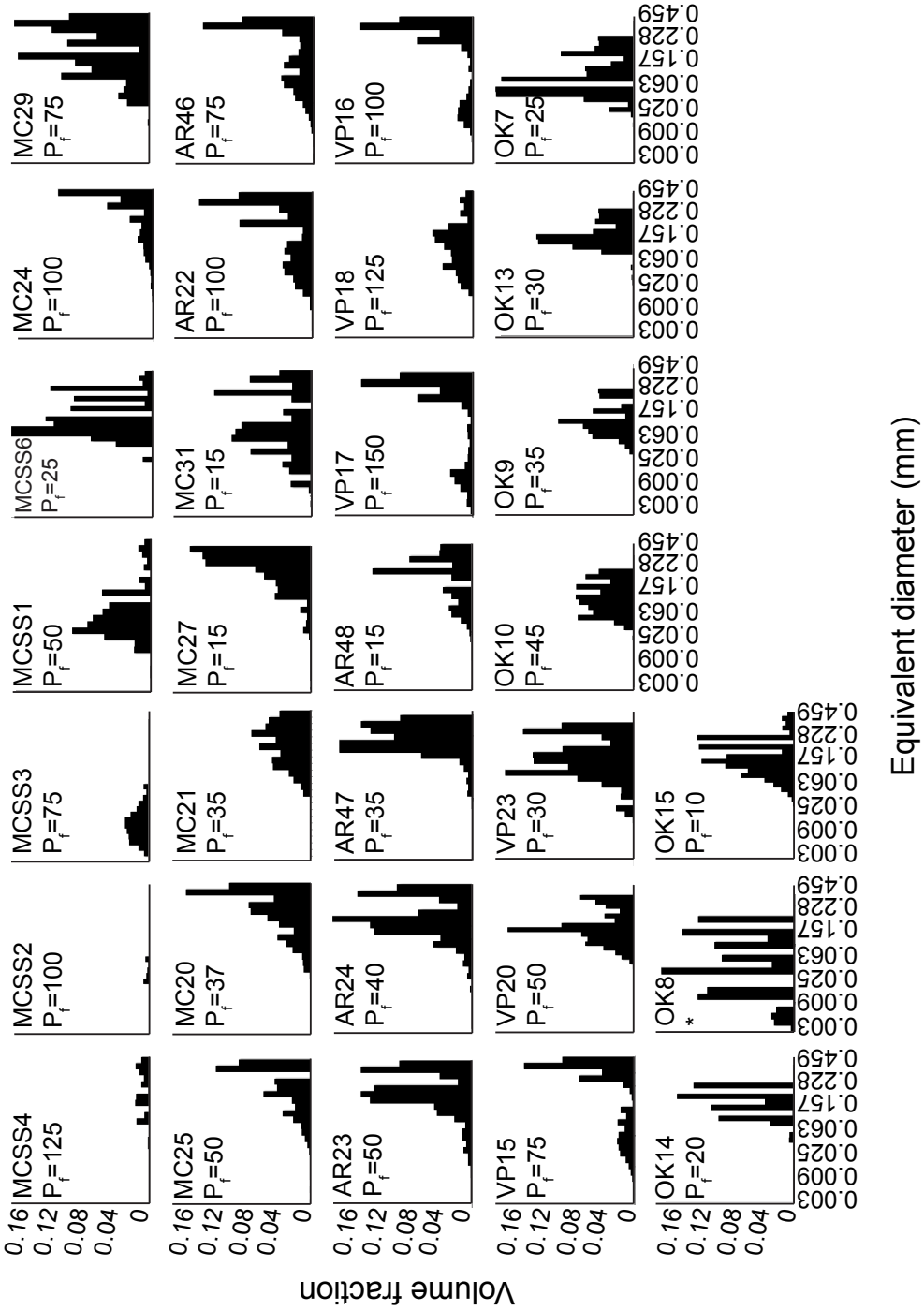

Fig.5: Bubble size distributions measured from rhyolite(MCSS and MC), rhyodacite (AR), K-phonolite (VP), and basaltic andesite (BA) samples. Volume fractions sum to vesicularity for each sample**.** * = 10 MPa.

Another interesting observation in the rhyolite samples is that porosity decreases slightly with increasing permeability. We interpret this observation to reflect the degassing process. Once an aperture has formed between two coalescing bubbles, overpressure within the bubbles decreases (Namiki and Kagoshima, 2014). The pressure loss within a bubble due to aperture formation can be approximated as (Namiki and Kagoshima, 2014):

$$p = p_o \exp\left[\frac{\pi P_a r_o^2}{\rho_g c_g V}\frac{\eta e}{2\sigma}\left\{1 - \exp\left(\frac{2t\sigma}{\eta e}\right)\right\}\right], \quad (3)$$

where p_o is the internal bubble pressure estimated using the Rayleigh-Plesset equation, P_a is atmospheric pressure (10^5 Pa), r is the initial aperture radius, η and σ are the viscosity and surface tension of the melt. To model bubble pressure loss, the film thickness (e) was calculated using the relationship found by Namiki and Kagoshima (2014), such that $e \propto \eta^{-0.62}$. We used values determined by Kobayashi et al. (2010) for a supercritical gas of density (ρ_g) 0.16 kg m^{-3} and sound velocity (c_g) of 870 m s^{-1}. We used an average decompression bubble size of 24 μm and calculated pressure loss within rhyolite (η=$10^{5.5}$, σ=0.11 N m^{-1}) (Mangan and Sisson, 2000), K-phonolite (η= $10^{4.3}$, σ= 0.063 N m^{-1}) (Iacono-Marziano et al., 2007), and basaltic andesite (η=10^2 Pa s, σ=0.09 N m^{-1}) (Khitarov et al., 1979) melt at approximately 800 m depth. We found it takes longer to relieve overpressure in high viscosity magma, mainly because aperture growth is slower. As pressure decreases in the bubble, the aperture retracts until tensional force is lost due to pressure release (Kobayashi et al., 2010). Depending on the stability of the bubbly

294 melt, gas loss may result in melt deformation and some degree of bubble shrinkage
295 (Burgisser and Gardner, 2004; Mongrain et al., 2008). Alternatively, external pressure
296 acting on the melt may cause bubbles to partially or completely resorb (Eichelberger et
297 al., 1986; Martel and Iacono-Marziano, 2015). It is likely that the relatively higher
298 external pressure of the melt would have influenced the porosities of this study had we
299 allowed a longer holding time at final quench pressures. However, samples were
300 quenched approximately 15 seconds after final pressures were reached. This short hold
301 time and fast quench time (~2.2 s) would not have allowed bubbles in the silicic
302 experiments to relax, with the exception of the basaltic andesite melts. Therefore the
303 permeable network achieved in the silicic melts would have persisted until quench.
304
305 *4.2. Degassing in rhyolite, rhyodacite and K-phonolite melts*
306 We found it important to confirm the degassing histories of the silicic experiments
307 using FTIR methods, because the presence of hydration bubbles affected the
308 interpretation of porosity measurements. All of the rhyolite and rhyodacite samples are
309 supersaturated, which indicates disequilibrium degassing (Fig. 2). Oversaturation is not
310 unusual for rhyolitic melts, as it is difficult for silica-rich melts to degas efficiently at fast
311 decompression rates (>0.25 MPa/s; Gardner et al., 1999; Burgisser and Gardner, 2004).
312 At the moderate decompression rates of our experiments (0.25 MPa/s), the degree of
313 oversaturation that we see is somewhat less than that observed by Gardner et al. (1999),
314 perhaps because of the higher experimental temperature employed in our study (900°C
315 vs. 825°C), which should both lower melt viscosity and enhance water diffusion. The K-
316 phonolite samples, in contrast, are in good agreement with equilibrium solubilities,

317 consistent with a previous study, which showed that K-phonolite could degas efficiently
318 even at high decompression rates (0.25 MPa/s; Mongrain et al., 2008).
319
320 *4.3. Degassing in basaltic andesite melts*
321 By comparison with the silicic samples, basaltic andesite samples from both
322 powdered and solid slab experiments behave very differently during decompression.
323 Although they vesiculate and achieve a porosity of 63 vol. % at final pressures of 10
324 MPa, none of the basaltic andesite samples had measurable permeabilities (Fig. 3). In
325 order to understand the cause of apparent impermeability, it is important to note that the
326 basaltic andesite porosities are systematically lower than predicted for equilibrium
327 exsolution using equation 2. We consider three possible explanations for the low
328 porosities, which will be addressed throughout the remainder of this section: 1)
329 disequilibrium exsolution 2) bubble rise out of the sample during decompression or 3)
330 development of permeable pathways leading to melt degassing, porosity reduction, and
331 rapid re-annealing of pore throats between connected bubbles due to short melt relaxation
332 times.
333 Disequilibrium H_2O exsolution is unlikely in basaltic andesite melts, as water can
334 diffuse 30 to 50 times faster than in rhyolites. Indeed, the μ-FTIR data plotted in Figure 2
335 show that quenched basaltic andesite glasses from our experiments have dissolved water
336 concentrations that agree very well with the calculated solubility curve. This rules out
337 disequilibrium exsolution as the explanation for the systematically low porosities and
338 negligible permeability.

339 The low melt viscosities (10^2 to 10^3 Pa s) of the basaltic andesite suggest that low
340 porosities could record bubble rise out of the sample into the capsule headspace. We test
341 this hypothesis by determining the rise velocity (v) for a spherical bubble using Stokes
342 Law:
343
344 (4) $$v = \frac{2}{9\eta}(r^2 g(\rho_b - \rho_m)),$$
345
346 where η is the viscosity of the melt, r is the bubble radius, g is the gravitational constant,
347 ρ_b and ρ_m are the densities of the gas and melt, respectively. At 900°C and 150 MPa, the
348 estimated water content of Okmok basaltic andesite is 4.36 wt. % (Moore et al., 1998),
349 and the melt viscosity under these conditions is 10^2 Pa s according to the model of
350 Giordano et al. (2008). For a melt density of 2650 kg m^{-3} and an average bubble radius of
351 24 μm, equation 4 predicts a bubble rise rate of 1.67x10^{-5} mm/s. During decompression,
352 even as the bubbles grow larger, this rate would have slowed as the melt became more
353 viscous during water exsolution (Fig. 6). The range of bubble rise velocities estimated
354 using hydration and decompression bubble average radii allows us to estimate the time
355 required for a bubble to escape from the upper 1/3 of the capsule. Given that the average
356 length of the experimental charges is 10 mm and the longest decompression timescale is
357 9.5 minutes, small bubbles would not be able to escape from the melt. However, some
358 hydration bubbles ($r \approx 50\ \mu m$) with faster rise rates (~1.39x10^{-4} mm/s) might have been
359 able to escape the melts during the average initial holding time of 2.25 hours (8100
360 seconds). Bubble loss to the headspace at the top of the capsule would explain why using
361 a powdered starting material for basaltic andesite runs does not inflate the measured

362 porosity. In contrast, bubble rise in our silicic experiments is negligible. For example, a
363 bubble 24 μm in diameter in a rhyolite melt with a viscosity of 4.16 Pa s and density of
364 2300 kg m^{-3} has a rise velocity of $1.83x10^{-7}$ mm/s. We conclude that the resulting
365 porosities in all experiments, even the low viscosity basaltic andesite runs, were not
366 affected by bubble rise during decompression except for possible loss of hydration
367 bubbles from the more mafic melts (Fig.6).

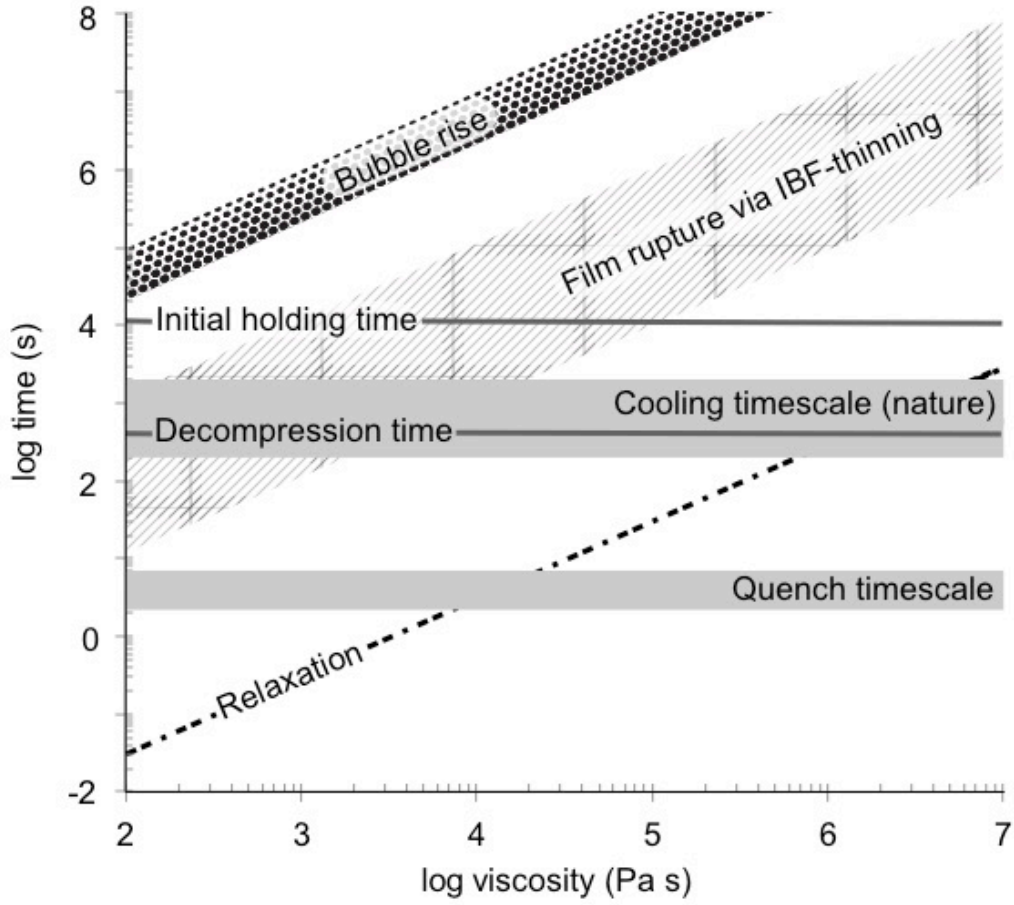

Fig. 6: Compilation of possible factors influencing recorded vesicularities and permeabilities in our experiments including: bubble rise velocities, melt relaxation timescale, film rupture via film thinning, as well as quench and cooling timescales all as a function of melt viscosity. A range of bubble rise velocities was estimated using hydration and decompression bubble average radii (see Discussion section 4.3). The velocities were then used to approximate the amount of time required for a bubble to escape the upper 1/3 of the capsule. Film rupture timescales were calculated using different values for critical film thicknesses. The top gray bar represents the

cooling timescale of natural pyroclasts (Szramek et al., 2010). The bottom gray bar represents the estimated quench timescale (2.2-6.5 s) of experiments. The initial holding time and maximum decompression time are marked with lines. Note the basaltic andesite relaxation timescale is faster than the quench timescale. Basaltic andesite, K-phonolite and rhyolite relaxation timescales are generally faster than natural cooling rates, with the exception of rhyolite melts at low final pressures (high melt viscosity).

Our preferred hypothesis to explain lower-than-equilibrium porosities and lack of measureable permeability in the basaltic andesites is syn- and post-decompression degassing. Even though we employed rapid quench methods and expect that the sample cooled to the glass transition temperature within a few seconds (Gardner et al., 1999; McIntosh et al., 2014), the short melt relaxation timescales could have allowed melt drainage into, or collapse of, the bubble walls, thus lowering the porosity; resulting reduction of pore apertures would also reduce the permeability. We can test this hypothesis by calculating the melt relaxation timescale of our basaltic andesite melt and comparing it to the quench time. The timescale for a bubble to return to a relaxed, spherical shape can be calculated after Toramaru, (1988):

$$\tau_r \approx \eta a / \sigma, \quad (5)$$

where η is the melt viscosity, a is the bubble radius and σ is the surface tension. Using the calculated viscosity (10^3 Pa s) of basaltic andesite at the lowest final pressure (10 MPa) and a surface tension of 0.09 N/m (Khitarov et al., 1979), we find a relaxation time is 0.3 seconds for a bubble with a radius of 30 μm (Fig. 6). This relaxation timescale is much faster than the cooling time of the quenched charge (~2.2 – 6.5 s; Gardner et al., 1999; Castro et al., 2012b; McIntosh et al., 2014). Because water content decreases melt viscosity, relaxation would occur faster at higher final pressures when more water resides

388 in the melt (Fig. 6). The surface tension of basaltic andesite is not well constrained, but
389 increasing surface tension only shortens the resulting timescale. For example, a surface
390 tension of 0.25 N m^{-1} (Murase and McBirney, 1973) reduces the relaxation timescale to
391 0.1 seconds. From this we conclude that, it is difficult to preserve the structure of the
392 vesicular basaltic andesite samples during quenching, without significant modifications.
393 The simplest explanation for the observed lack of measurable permeability is that
394 the samples became permeable, degassed, and then relaxed to a less porous and
395 impermeable state before quenching. For samples decompressed to 10 MPa, this requires
396 that the percolation threshold was reached at a vesicularity greater than 63 vol. %. This
397 suggests that the basaltic andesite melts also required high porosities for permeability to
398 develop. Once permeability is achieved, however, they are able to outgas much more
399 quickly than high viscosity melts. Film rupture timescales provide the greatest control on
400 this process, as inter-bubble melt films (IBFs) must rupture to form an aperture through
401 which gas can move. This can occur via mechanisms such as capillary drainage,
402 stretching via expansion, or dimpling (Castro et al., 2012b). We have calculated the time
403 (τ_f) required for melt to drain from an initial thickness (δ_f) to a critical thickness (δ_{cr})
404 from the binary coalescence model of Proussevitch et al., (1993):
405
406 (6) $$\tau_f = \frac{3\eta R^3}{4\sigma}\left(\frac{1}{\delta_{cr}^2} - \frac{1}{\delta_f^2}\right),$$
407
408 We use our experimental viscosity range of 10^2-$10^{6.2}$ Pa s, surface tensions defined above,
409 an initial thickness of 10 μm and critical rupture thicknesses between 0.1 – 1μm (Klug et
410 al., 2002; Castro et al., 2012b). The uncertainty linked with initial and critical thicknesses

411 results in the large range of thinning timescales (Fig. 6). We obtain similar timescales as
412 reported in Castro et al., (2012b) in that low viscosity melts (10^2 Pa s) will thin to critical
413 thicknesses within 100 seconds. As seen in Figure 6, the basaltic andesite melts could
414 have coalesced via melt-film drainage over the course of the decompression time (570
415 seconds). However, IBFs in high viscosity melts take orders of magnitude longer to thin
416 (10^3-10^7 seconds). The K-phonolite, rhyodacite, and rhyolite melts would not be able to
417 coalesce by melt-film thinning alone, but instead would require faster film rupture
418 mechanisms, such as IBF stretching due to bubble growth or dimpling (Castro et al.,
419 2012b).

420 A percolation threshold in excess of 63 vol. % for the low viscosity melts is
421 consistent with the percolation threshold > 65 vol. % observed by Namiki and Manga,
422 (2008) for low viscosity analog materials. The evidence we have discussed in the
423 following section demonstrates that it is likely our experiments achieved permeability
424 during decompression, but given limitations inherent to the cold-seal hydrothermal
425 experimental apparatus and design, it is very difficult to constrain the percolation
426 threshold in mafic melts, and make it difficult to compare the results directly with the
427 silicic experiments (Fig. 3).

428

429 *4.4. Melt viscosity and its control on percolation threshold*

430 To assess the control of melt viscosity on permeability development, we
431 calculated viscosities of the silicic experimental melts at the observed percolation
432 thresholds. Melt viscosities of rhyolite, rhyodacite, and k-phonolite are $10^{5.5}$, 10^5, and
433 $10^{4.6}$ Pa s at critical porosities of 68.3(2.2), 77.3(0.4) and 75.6(1.9) vol. %, respectively.

As described above, the basaltic andesite samples likely became permeable at porosities greater than 63 vol. % at a viscosity of about 10^3 Pa s (Fig. 7). If we interpret 63 vol. % as a lower bound for permeability development, our data suggests melt viscosity alone does not greatly influence the percolation threshold.

The consistency of percolation thresholds of high viscosity melts implies that silicic, crystal-free systems require high vesicularities to become permeable. Interestingly, our findings suggest low viscosity melts may require similarly high porosities for permeability development. Although the fast melt relaxation timescales appear to have hindered our ability to capture the percolation threshold, our results, in combination with those from analog materials (~70 vol. %; Namiki and Manga, 2008), support this hypothesis. In crystal-free melts, permeability development depends on bubble coalescence (Blower, 2001). Coalescence by film drainage requires that melt films thin to the point of rupture; for this to happen, the bubbles must be close enough to "feel" and do mechanical work on each other. Because the drainage time is a function of melt viscosity (Eq. 6), aperture formation, and thus outgassing rates, will be delayed in high viscosity melts (Proussevitch et al., 1993; Gonnermann and Manga, 2007; Namiki and Kagoshima, 2014). Mafic melts also require high vesicularities for degassing to commence on the decompression timescales of our experiments, however, rapid film drainage will aid aperture enlargement, cause permeability to increase rapidly and allow efficient syn-decompression degassing and reduction of gas overpressures. In this way, degassing of mafic melts is not bound by the same kinetic limitations as silicic melts.

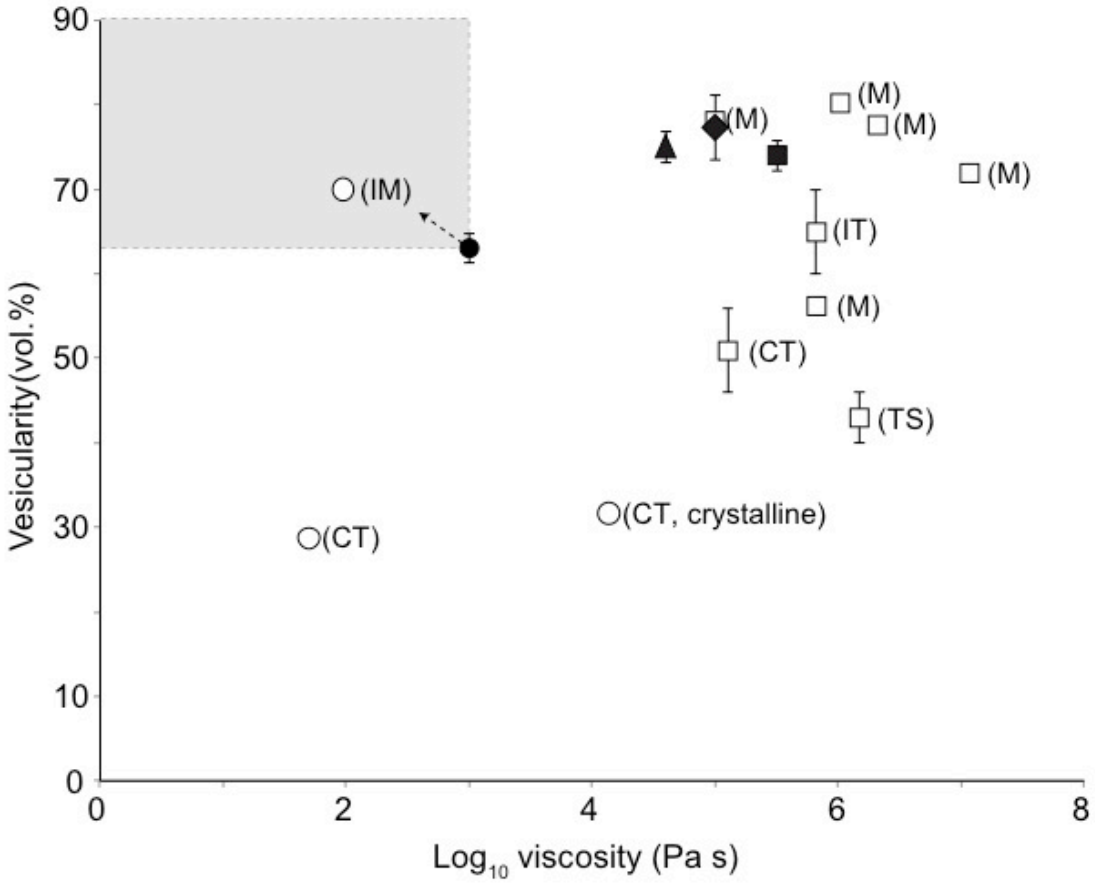

Fig. 7: Comparison of percolation thresholds as a function of melt viscosity between this study (black square, diamond, triangle and circle corresponding to the same compositions as previous labels) and previous studies of permeability development in natural and experimental systems (open squares and circles based on composition)(Eichelberger et al., 1986; Westrich and Eichelberger, 1994; Klug and Cashman, 1996; Burgisser and Gardner, 2004; Namiki and Manga, 2008; Nakamura et al., 2008; Takeuchi et al., 2009, Bouvet de Maisonneuve et al., 2009; Bai et al., 2010, 2011; Martel and Iacono-Marziano, 2015) . Notes next to data points refer to how permeability was estimated (M = permeameter measurement, CT = X-ray Computed Tomography, TS = inferred from thin-section analysis, IT = inferred from isotopic tracer, IM = indirectly measured via density, mass and height measurements). Measured porosities of silicic systems group above 70 vol. % for high melt viscosities, while calculated or lattice Boltzmann simulations produce lower vesicularities for comparable viscosities. We predict the percolation threshold for crystal-free basaltic andesite lies within the shaded region.

455 *4.5 Potential effects of viscosity on eruptive style*

456 In silicic magma, where bubble nucleation, growth and coalescence is often
457 delayed (e.g., Mangan and Sisson, 2000), the vesicularity needed for permeability
458 development may not be achieved until the magma reaches shallow depths. For this
459 reason, degassing efficiency is strongly controlled by the timescales of decompression
460 (Martel and Iacono-Marziano, 2015). Rhyolite magmas ascending at the fast rates studied
461 here would not outgas fast enough to relieve overpressure, and therefore would culminate
462 in an explosive eruption. Bubble coalescence is expected to be faster in lower viscosity
463 melts. Our experiments support this: although high vesicularities are required for
464 permeability to develop, the mafic melts outgas rapidly, followed by collapse of the
465 permeable networks. This hysteresis effect, where vesicularity decreases during
466 outgassing, is typically observed in effusive products (e.g., Rust and Cashman, 2004;
467 Mueller et al. 2008). Our experiments show that, in contrast, mafic magmas could
468 experience this effect even with the fast ascent that characterizes explosive eruptions.

469 This raises a final question, which relates to controls on magma explosivity. The
470 decompression rates employed here are rapid, and faster than inferred for most conditions
471 of magma ascent, and reflecting instead conditions achieved by rapid downward-
472 propagating decompression waves. Efficient syn-decompression degassing under these
473 conditions underlines the difficulty in generating explosive eruptions from low viscosity
474 and low crystallinity magma. One suggested mechanism of retaining gas pressure in
475 mafic melts is to increase the viscosity by microlite crystallization driven by degassing
476 during magma ascent (e.g., Houghton and Gonnermann, 2008). Importantly, this
477 mechanism requires both gas exsolution from the melt and then sufficient time for

crystals to nucleate and grow. Our experiments support those of Szramek et al., (2006) and observations of Wright et al., (2012), which suggest that decompression-driven crystallization of water-saturated basaltic andesite requires decompression rates of < 10 MPa/s. Interestingly, explosively erupted mafic samples with high crystallinities commonly also have low preserved vesicularities (Pioli et al., 2008; Vinkler et al., 2012). These observations support our interpretation of the degassing efficiency of mafic magma, as well as the role of ΔP (difference between magma pressure and the surface) in driving explosive mafic eruptions (Cashman and Giordano, 2014).

5. Summary

This study constrains the onset of permeability development in crystal-free rhyolite, rhyodacite, K-phonolite, and basaltic andesite melts using high pressure and temperature, isothermal decompression experiments. Bubbles in rhyolite, rhyodacite, and K-phonolite melts underwent extensive coalescence culminating in permeability development at vesicularities of ~70-75 vol.%. Internal pressures within bubbles is subsequently reduced following gas loss, which causes porosities to decrease slightly, although permeability is still maintained. Quenched silicic experimental products record viscous permeability values similar to previous experimental studies of silicic melts (e.g., Takeuchi et al., 2009) and measurements of silicic pumice (Klug and Cashman, 1996; Rust and Cashman, 2011).

Basaltic andesite samples are not measurably permeable but show evidence of melt degassing, in that measured water contents agree with calculated water solubility but measured porosities are consistently lower than calculated equilibrium values. Stokes

501 velocities negate the possibility of degassing via bubble rise over the short experimental
502 timescale. Therefore we assume the basaltic andesite melts degassed. Estimated film
503 rupture timescales are shorter than experimental timescales, which shows that degassing
504 of the basaltic melts is possible. The degassing resulted in porosity reduction and closure
505 of bubble apertures, which consequently sealed off degassing pathways and substantially
506 reduced permeability. Although we cannot constrain the percolation threshold for basaltic
507 andesite melts due to extremely fast melt relaxation times (<0.3 seconds at a viscosity
508 less than 10^3 Pa s), we assume that the percolation threshold is higher than the maximum
509 porosity measured (63 vol. %).
510 The similarity between silicic and mafic percolation thresholds observed
511 experimentally in this study indicates melt viscosity has no effect on the percolation
512 threshold. However, it is clear from our experiments that melt viscosity does influence
513 outgassing behavior. Contrary to predictions, we do not see a significant increase in
514 percolation threshold vesicularity between melt viscosities of 10^3 and $10^{4.6}$ Pa s. The
515 coherence of silicic and mafic percolation thresholds (Fig. 7) implies that under
516 conditions of rapid decompression, permeability can develop in crystal-free melts only at
517 high melt vesicularities (>60 vol. %). Permeability at lower vesicularities in such magmas
518 requires another (hysteretic) mechanism, such as the presence of crystals, magma
519 shearing, micro-cracks, or post-fragmentation processes.

Acknowledgements: We would like to thank Caroline Martel and an anonymous reviewer for their comments, which have greatly improved this paper. We would also like to thank Lucia Gurioli and Thomas Shea for providing the Vesuvius EU2 samples. This study was

supported by a grant from the National Science Foundation (NSF EAR 1145194 to JL) and awards from the AXA Research Fund and Royal Society (to KC).

Appendix A. Supplementary material

Table 1: Major oxide compositions of starting materials

Oxide	MC[1]	AnRd[2]	VP[3]	OK52A[4]
SiO_2	76.32(0.29)	70.57	55.41(0.38)	54.82(0.51)
TiO_2	0.21(0.17)	0.53	0.26(0.11)	2.55(0.5)
Al_2O_3	13.02(0.06)	15.31	21.97(0.45)	14.49(0.2)
FeO*	1.03(0.08)	2.69	2.90(0.38)	11.03(0.23)
MnO	-	0.16	0.24(0.12)	0.18(0.06)
MgO	0.04(0.02)	0.61	0.65(0.07)	3.38(0.09)
CaO	0.53(0.03)	2	3.69(0.25)	7.36(0.47)
Na_2O	3.93(0.11)	5.38	5.32(0.21)	4.16(0.26)
K_2O	4.73(0.10)	2.97	9.17(0.39)	1.28(0.1)
Cl	-	-	0.26(0.14)	-
P_2O_5	-	0.11	0.12(0.05)	-
Total	100	99.6	99.76(0.58)	99.25
n[5]	4	1	19	4

[1]Mono Craters rhyolite. EPMA analysis.
[2]Aniakchak rhyodacite. XRF analysis (Larsen, 2006)
[3]EU2 Vesuvius 79AD k-phonolite. EPMA analysis (Shea et al., 2010)
[4]Okmok basaltic andesite. EPMA analysis (Wong and Larsen, 2009).
[5]Number of analyses

References

Bai, L., Baker, D.R., Hill, R.J., 2010. Permeability of vesicular Stromboli basaltic glass: lattice Boltzmann simulations and laboratory measurements. J. Geophys. Res. 115, B07201. DOI: 10.1029/2009JB007047

Blower, J., 2001. Factors controlling permeability–porosity relationships in magma. Bull. Volcanol. 63, 497-504. DOI:10.1007/s004450100172

Burgisser, A., and Gardner, J. E., 2004. Experimental constraints on degassing and permeability in volcanic conduit flow. Bull. Volcanol. 67, 42-56. DOI: 10.1007/s00445-004-0359-5

Cashman, K. V., & Giordano, G., 2014. Calderas and magma reservoirs. J. Volcanol. Geotherm. Res., 288, 28-45.

Castro, J. M., Cordonnier, B., Tuffen, H., Tobin, M. J., Puskar, L., Martin, M. C., and Bechtel, H. A., 2012a. The role of melt-fracture degassing in defusing explosive rhyolite eruptions at volcán Chaitén. Earth Planet. Sci. Lett. 333, 63-69. DOI:10.1016/j.epsl.2012.04.024

Castro, J. M., Burgisser, A., Schipper, C. I., and Mancini, S. 2012b. Mechanisms of bubble coalescence in silicic magmas. Bull. Volcanol., 74, 2339-2352.

Eichelberger, J. C., Carrigan, C. R., Westrich, H. R., and Price, R. H., 1986. Non-explosive silicic volcanism. Nature 323, 598-602.

Gardner, J.E., Hilton, M., and Carroll, M.R., 1999. Experimental constraints on degassing of magma: isothermal bubble growth during continuous decompression from high pressure. Earth and Planet. Science Lett. 168, 201-218. DOI:10.1016/S0012-821X(99)00051-5

Giordano, D., Russell, J. K., and Dingwell, D. B., 2008. Viscosity of magmatic liquids: a model. Earth Planet. Sci. Lett. 271, 123-134. DOI:10.1016/j.epsl.2008.03.038

Gonnermann, H.M., and Manga, M., 2007. The fluid mechanics inside a volcano. Annu. Rev. Fluid Mech. 39, 321–356. DOI: 10.1146/annurev.fluid.39.050905.110207

Houghton, B. F., and Gonnermann, H. M., 2008. Basaltic explosive volcanism: constraints from deposits and models. *Chem. Erde-Geochem.*, *68*, 117-140.

Iacono-Marziano, G., Schmidt, B. C., & Dolfi, D., 2007. Equilibrium and disequilibrium degassing of a phonolitic melt (Vesuvius AD 79 “white pumice”) simulated by decompression experiments. J.Volcanol. Geotherm. Res., 161, 151-164.

Jaupart, C., 1998. Gas loss from magmas through conduit walls during eruptions, Geo.

Soc. Lond. Spec. Pub. 145, 73-90.

Khitarov, N.I., Lebedev, Ye.B., Dorfman, A.M., Bagdasarov, N.Sh., 1979. Effects of temperature, pressure, and volatiles on the surface tension of molten basalt. Geochem. Int. 16, 78–86.

King, P. L., Ramsey, M. S., McMillan, P. F., and Swayze, G. 2004. Laboratory Fourier transform infrared spectroscopy methods for geologic samples. Infrared Spectroscopy in Geochemistry, Exploration Geochemistry and Remote Sensing; King, PL, Ramsey, MS, McMillan, PF, Swayze, GA, Eds, 57-91.

Klug, C., and Cashman, K. V., 1996. Permeability development in vesiculating magmas: implications for fragmentation. Bull. Volcanol. 58, 87-100. DOI:10.1007/s004450050128

Klug, C., Cashman, K., and Bacon, C., 2002. Structure and physical characteristics of pumice from the climactic eruption of Mount Mazama (Crater Lake), Oregon. Bull. Volcanol. 64, 486-501.

Larsen, J.F., and Gardner, J.E., 2000. Experimental constraints on bubble interactions in rhyolite melts: implications for vesicle size distributions. Earth Planet. Sci. Lett. 180, 201-214. DOI:10.1016/S0012-821X(00)00166-7

Larsen, J.F., 2006. Rhyodacite magma storage conditions prior to the 3430 yBP caldera-forming eruption of Aniakchak volcano, Alaska. Cont. Mineral. Petrol. 152, 523-540. 10.1007/s00410-006-0121-4

Mangan, M., and Sisson, T., 2000. Delayed, disequilibrium degassing in rhyolite magma: decompression experiments and implications for explosive volcanism. Earth Planet. Sci. Lett. 183, 441-455. DOI:10.1016/S0012-821X(00)00299-5

Martel, C., and Iacono-Marziano, G., 2015. Timescales of bubble coalescence, outgassing, and foam collapse in decompressed rhyolitic melts. Earth Planet. Sci. Lett. 412, 173-185. DOI:10.1016/j.epsl.2014.12.010

Mongrain, J., Larsen, J. F., and King, P. L., 2008. Rapid water exsolution, degassing, and bubble collapse observed experimentally in K-phonolite melts. J. Volcanol. Geotherm. Res. 173, 178-184. DOI:10.1016/j.jvolgeores.2008.01.026

Murase, T., and McBirney, A.R., 1973. Properties of some common igneous rocks and their melts at high temperatures. GSA Bull. 84, 3563-3592. DOI: 10.1130/0016-7606(1973)84<3563:POSCIR>2.0.CO;2

Moore, G., Vennemann, T., and Carmichael, I. S. E., 1998. An empirical model for the solubility of H2O in magmas to 3 kilobars. Am. Mineral. 83, 36-42.

Mueller, S., Scheu, B., Spieler, O., and Dingwell, D. B., 2008. Permeability control on magma fragmentation. Geology 36, 399-402. DOI: 10.1130/G24605A.1

Namiki, A., Manga, M., 2008. Transition between fragmentation and permeable outgassing of low viscosity magmas. J. Volcanol. Geotherm. Res. 169, 48-60. DOI:10.1016/j.jvolgeores.2007.07.020

Namiki, A., and Kagoshima, T., 2014. Intermittent and efficient outgassing by the upward propagation of film ruptures in a bubbly magma. J. Geophys. Res. 119, 919-935. DOI: 10.1002/2013JB010576

Okumura, S., Nakamura, M., Nakano, T., Uesugi, K., and Tsuchiyama, A., 2012. Experimental constraints on permeable gas transport in crystalline silicic magmas. Cont. Mineral. Petrol. 164, 493-504. DOI:10.1007/s00410-012-0750-8

Pioli, L., Erlund, E., Johnson, E., Cashman, K., Wallace, P., Rosi, M., and Granados, H. D., 2008. Explosive dynamics of violent Strombolian eruptions: the eruption of Parícutin Volcano 1943–1952 (Mexico). Earth Planet. Sci. Lett., 271, 359-368. DOI:10.1016/j.epsl.2008.04.026

Polacci, M., Baker, D. R., La Rue, A., Mancini, L., and Allard, P., 2012. Degassing behaviour of vesiculated basaltic magmas: an example from Ambrym volcano, Vanuatu Arc. J. Volcanol. Geotherm. Res. 233, 55-64. DOI:10.1016/j.jvolgeores.2012.04.019

Polacci, M., de Maisonneuve, C. B., Giordano, D., Piochi, M., Mancini, L., Degruyter, W., & Bachmann, O. (2014). Permeability measurements of Campi Flegrei pyroclastic products: An example from the Campanian Ignimbrite and Monte Nuovo eruptions. J.Volcanol.Geotherm. Res.,272, 16-22. DOI:10.1016/j.jvolgeores.2013.12.002

Proussevitch, A.A., Sahagian, D.L., Kutolin, V. A., 1993. Stability of foams in silicate melts, J. Volcanol. Geotherm. Res. 59, 161-178. DOI:10.1016/0377-0273(93)90084-5

Rust, A. C., and Cashman, K. V., 2004. Permeability of vesicular silicic magma: inertial and hysteresis effects. Earth Planet. Sci. Lett. 228, 93-107. DOI:10.1016/j.epsl.2004.09.025

Rust, A. C., and Cashman, K.V., 2011. Permeability controls on expansion and size distributions of pyroclasts. J. Geophys. Res.: Solid Earth 116. DOI:10.1029/2011JB008494

Saar, M. O., and Manga, M., 1999. Permeability-porosity relationship in vesicular basalts. Geophys. Res. Lett. 26, 111-114. DOI: 10.1029/1998GL900256

Sahimi, M., 1994. Long-range correlated percolation and flow and transport in heterogeneous porous media. J. de Physique I 4, 1263-1268.

Shea, T., Gurioli, L., Larsen, J. F., Houghton, B. F., Hammer, J. E., and Cashman, K. V., 2010a. Linking experimental and natural vesicle textures in Vesuvius 79AD white pumice. J. Volcanol. Geotherm. Res. 192, 69-84. DOI:10.1016/j.jvolgeores.2010.02.013

Shea, T., Houghton, B. F., Gurioli, L., Cashman, K. V., Hammer, J. E., and Hobden, B. J., 2010. Textural studies of vesicles in volcanic rocks: an integrated methodology. J. Volcanol. Geotherm. Res.,190, 271-289. DOI:10.1016/j.jvolgeores.2009.12.003.

Stolper, E., 1982. The speciation of water in silicate melts. Geochim. Cosmochim. Acta, 46, 2609-2620.

Szramek, L., Gardner, J. E., and Larsen, J. (2006). Degassing and microlite crystallization of basaltic andesite magma erupting at Arenal Volcano, Costa Rica. J.Volcanol. Geotherm. Res., 157, 182-201.

Szramek, L., Gardner, J. E., and Hort, M., 2010. Cooling-induced crystallization of microlite crystals in two basaltic pumice clasts. Am. Mineral. 95, 503-509. DOI:10.2138/am.2010.3270

Takeuchi, S., Nakashima, S., and Tomiya, A., 2008. Permeability measurements of natural and experimental volcanic materials with a simple permeameter: toward an understanding of magmatic degassing processes. J. Volcanol. Geotherm. Res. 177, 329-339. DOI:10.1016/j.jvolgeores.2008.05.010

Takeuchi, S., Tomiya, A., and Shinohara, H., 2009. Degassing conditions for permeable silicic magmas: Implications from decompression experiments with constant rates. Earth and Planet. Science Lett. 283, 101-110. DOI:10.1016/j.epsl.2009.04.001

Toramaru A, 1988. Formation of propagation pattern in two-phase flow systems with application to volcanic eruptions. J. Geophys., 95:613–623.

Westrich, H. R., and Eichelberger, J. C., 1994. Gas transport and bubble collapse in rhyolitic magma: an experimental approach. Bull. Volcanol. 56, 447-458. DOI:10.1007/BF00302826

Wong, L. J., and Larsen, J. F., 2010. The Middle Scoria sequence: A Holocene violent strombolian, subplinian and phreatomagmatic eruption of Okmok volcano, Alaska. Bull. Volcanol. 72, 17-31. DOI: 10.1007/s00445-009-0301-y

Wright, H.M.N., Cashman, K.V., Rosi, M., and Cioni, R., 2007. Breadcrust bombs as indicators of Vulcanian eruption dynamics at Guagua Pichincha volcano, Ecuador. Bull. Volcanol. 69, 281–300. DOI:10.1007/s00445-006-0073-6

Wright, H. M. N, Cashman, K.V., Gottesfeld, E. H., and Roberts, J. J., 2009. Pore structure of volcanic clasts: Measurements of permeability and electrical conductivity. Earth Planet. Sci. Lett. 280, 93–104. DOI:10.1016/j.epsl.2009.01.023

Wright, H. M., Cashman, K. V., Mothes, P. A., Hall, M. L., Ruiz, A. G., and Le Pennec, J. L., 2012. Estimating rates of decompression from textures of erupted ash particles produced by 1999–2006 eruptions of Tungurahua volcano, Ecuador. Geology, 40, 619-622. DOI: 10.1130/G32948.1

Vinkler, A. P., Cashman, K., Giordano, G., and Groppelli, G., 2012. Evolution of the mafic Villa Senni caldera-forming eruption at Colli Albani volcano, Italy, indicated by textural analysis of juvenile fragments. J.Volcanol. Geotherm. Res., 235, 37-54.